RSC Advances

Cite this: *RSC Advances*, 2012, **2**, 4648–4655

www.rsc.org/advances

**PAPER**

# Electrical properties, thermodynamic behavior, and defect analysis of $La_{n+1}Ni_nO_{3n+1+\delta}$ infiltrated into YSZ scaffolds as cathodes for intermediate-temperature SOFCs

**Seonyoung Yoo,[a] Sihyuk Choi,[a] Jeeyoung Shin,[b] Meilin Liu[c] and Guntae Kim*[a]**

***Received 5th March 2012, Accepted 6th March 2012***
**DOI: 10.1039/c2ra20402a**



## Introduction

A solid oxide fuel cell (SOFC) is an electrochemical device for chemical-to-electrical energy conversion with high efficiency, low emissions, and excellent fuel flexibility. The requirement for high operating temperatures (1073–1273 K) of conventional SOFCs, however, leads to notable problems such as high costs and high rates of degradation due to interactions between cell components during cell fabrication and operation. To overcome these problems, much effort has been devoted to lowering the SOFC operating temperature toward an intermediate range (873 to 1073 K). One of the challenges for IT-SOFC is to develop cathode materials with high electrocatalytic activity for oxygen reduction at these temperatures.[1–5]

While $La_{1-x}Sr_xMnO_3$ (LSM) has been widely used as a cathode material for SOFCs based on YSZ electrolytes at high temperatures,[3,4] it is inadequate for use in an intermediate temperature range due to reduced ionic and electronic conductivity and diminished catalytic activity at lower temperatures.[5–7]

Recently, mixed ionic and electronic conductors (MIECs) have received tremendous attention as potential cathodes for IT-SOFCs. MIECs based on transition metal (*e.g.* Mn, Fe, Co, and Ni) oxides have been extensively investigated. Among various MIECs, cobalt containing oxides showed superior electrocatalytic activity than oxides with predominant electronic conductivity (and little ionic conductivity) such as lanthanum manganese. In particular, $La_{1-x}Sr_xCo_{1-y}Fe_yO_{3-\delta}$ (LSCF)-based cathodes have attracted much attention for IT-SOFCs. However, the long-term stability of LSCF-based cathodes is still a concern.[6–8]

As a mixed conductor derived from the $K_2NiF_4$-type materials, $La_2NiO_4$ has attracted significant attention for possible application as IT-SOFC cathodes. Its advantages include high oxygen ionic and electronic conductivity, moderate thermal expansion coefficient (TEC), and high electrocatalytic activity toward oxygen reduction under oxidizing conditions.[9–11] Other materials such as lanthanum cobaltite perovskite also exhibit good conductivities; however, the large thermal expansion mismatch with other cell components may lead to thermo-mechanical problems.

Ruddlesden–Popper compounds are comprised of alternating perovskite and rock-salt layers, as shown in Fig. 1. The number of perovskite layers increases with $n$ in this structure, leading to the formation of higher order Ruddlesden–Popper phases, $La_3Ni_2O_7$ and $La_4Ni_3O_{10}$, which is argued to allow faster ionic and electronic transport.[6,11,12] These effects are primarily attributed to increased concentration of Ni–O–Ni bonds, which are responsible for electronic conduction due to progressive delocalization of the $p$-type electronic charge carriers, and enhanced vacancy-migration or oxygen ion diffusivity.[4,11,12] Currently, many of the studies on $La_{n+1}Ni_nO_{3n+1+\delta}$ ($n$ = 1, 2, or 3) focused on the structure and electrochemical properties of the bulk phases, with little attention to the basic thermodynamic properties. To date, the characteristics of $La_{n+1}Ni_nO_{3n+1+\delta}$ infiltrated into a scaffold of YSZ and the actual configuration of a porous cathode fabricated by infiltration, are still unknown. Because of the unique microstructures and possible interactions between the two phases, the behaviour of this $La_{n+1}Ni_nO_{3n+1+\delta}$–YSZ could be very different from that of a pure $La_{n+1}Ni_nO_{3n+1+\delta}$ phase. Further, redox properties related to oxygen thermodynamics such as oxidation enthalpies and entropies of $La_{n+1}Ni_nO_{3n+1+\delta}$ ($n$ = 1, 2, and 3), and redox stability have not been reported for the intermediate temperature range.

In this study, we characterized non-stoichiometric variations of oxygen and electrical conductivities of $La_{n+1}Ni_nO_{3n+1+\delta}$ ($n$ = 1, 2, and 3) infiltrated into porous YSZ as a function of oxygen partial pressure in a temperature range of 923–1023 K. Redox behavior was evaluated using coulometric titration and the electrical conductivity was determined using 4-probe conductivity measurement.

## Experimental

$La_{n+1}Ni_nO_{3n+1}$ ($n$ = 1, 2, and 3)–YSZ slabs were prepared by the infiltration of $La_{n+1}Ni_nO_{3n+1}$ ($n$ = 1, 2, and 3) into a porous YSZ (Tosoh corp. TZ-8Y) slab. The porous YSZ slab was prepared by mixing YSZ powder, dispersant (Duramax3005, Rohm & Haas), binder (HA-12 and B-1000, Rohm & Haas), and pore former (graphite, Alfa Aeser, 325 mesh). This solution of YSZ

[a]*Interdisciplinary School of Green Energy, and KIER-UNIST Advanced Center for Energy, Ulsan National Institute of Science and Technology (UNIST), Ulsan, 689-798, Korea. E-mail: gtkim@unist.ac.kr; Fax: +82 52 217 2909.*
[b]*Department of Mechanical Engineering, Dong-Eui University, 995 Eomgwangno, Busan-jin-gu, Busan, 614-714, Korea.*
[c]*School of Materials Science and Engineering, Georgia Institute of Technology, 771 Ferst Drive, N.W., Atlanta, GA, 30332-0245, USA.*

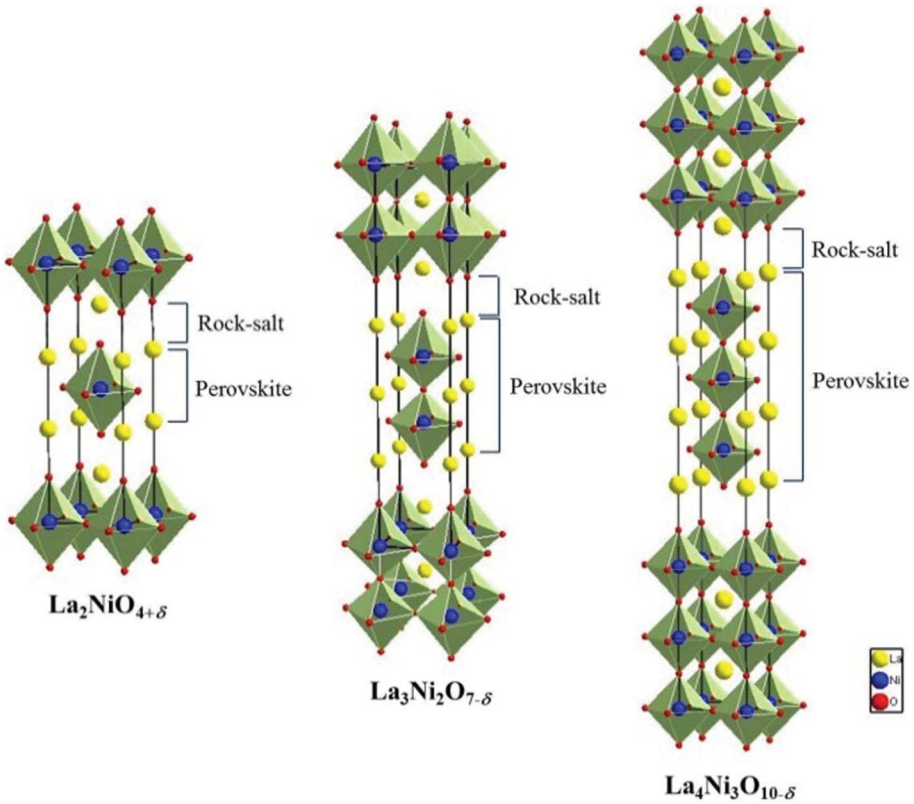


**Fig. 1** The structure of $La_{n+1}Ni_nO_{3n+1}$ ($n$ = 1, 2, and 3).

slurry was dried and sintered afterwards at 1773 K to yield porous YSZ with 65% porosity. Stoichiometric amounts of $La(NO_3)_3{\cdot}6H_2O$ (Aldrich, 99.9%), $Ni(NO_3)_2{\cdot}6H_2O$ (Aldrich), and citric acid were dissolved in distilled water, which were infiltrated into the porous YSZ up to higher than 45 wt% loading. After firing in air at 723 K and 1123 K, a $La_{n+1}Ni_nO_{3n+1}$ ($n$ = 1, 2, and 3) phase was formed in the porous YSZ.

The $La_{n+1}Ni_nO_{3n+1}$ ($n$ = 1, 2, and 3) were characterized using X-ray diffraction (XRD) and scanning electron microscopy (SEM). X-Ray powder diffraction measurements (Rigaku diffractometer, Cu Ka radiation) were performed to confirm the structure with a scan rate of 0.5° $min^{-1}$ and a range of $20° < 2\theta < 60°$.

The oxidation/reduction state can be characterized precisely by coulometric titration as a function of $p(O_2)$.[13,14] This involves placing the oxide sample in a sealed container, separated from the atmosphere by an $O^{2-}$-conducting membrane such as yttria-stablized zirconia (YSZ). The YSZ tube (McDanel Advanced Ceramic Technologies, Z15410630) was used both to pump oxygen out of the system and to sense the equilibrium $p(O_2)$ inside the tube. $La_{n+1}Ni_nO_{3n+1}$ ($n$ = 1, 2, and 3) were located in a sealed container at various temperatures of interest and equilibrated by subjecting it to a flow of 5% $O_2$ in Ar. The sample was then isolated in the tube and the equilibrium $p(O_2)$ was measured with an oxygen sensor. Electrodes on both sides of the YSZ tube were used to measure the potential across the membrane, and the potential could be related to the $p(O_2)$ through the Nernst equation. A specific amount of charge could be passed across the tube using a BioLogic Potentiostat, with 1 coulomb of charge being equivalent to 2.6 μmol of $O_2$.

The electrical conductivity of the slabs, 2 mm × 5 mm × 10 mm in size, was measured in air by the four-probe method with a BioLogic Potentiostat. The measurements were performed starting from 1023 to 373 K with 323 K measurement intervals.

## Results and discussion

### 1. XRD and SEM

Shown in Fig. 2 are typical XRD patterns of $La_{n+1}Ni_nO_{3n+1}$ (42 wt%)–YSZ fired at 1123 K, suggesting that the $La_{n+1}Ni_nO_{3n+1}$ compounds have a Ruddlesden–Popper structure and the two main phases are $La_{n+1}Ni_nO_{3n+1}$ and YSZ without observable peaks of other phases. The XRD data suggest that there were no observable chemical reactions between $La_{n+1}Ni_nO_{3n+1}$ and YSZ under the processing conditions.

As is well known, the microstructure of an electrode may influence the reaction kinetics, charge and mass transport processes, and hence fuel cell performance. For example, three phase boundaries (TPBs) at the electrode/electrolyte interfaces are the most active sites for electrochemical reactions in SOFCs. Smaller grain size often results in longer TPB length and potentially higher electrochemical performance.[13] SEM images of the $La_{n+1}Ni_nO_{3n+1}$–YSZ fired at 1123 K are presented in Fig. 3a, b, and c, respectively, for $n$ = 1, 2, and 3. It is clearly seen that the grain size of the $La_{n+1}Ni_nO_{3n+1}$ becomes smaller with the increasing value of $n$.

### 2. Thermodynamic characterization

Shown in Fig. 4 are the equilibrium oxygen non-stoichiometries for $La_{n+1}Ni_nO_{3n+1}$ infiltrated in YSZ determined by coulometric

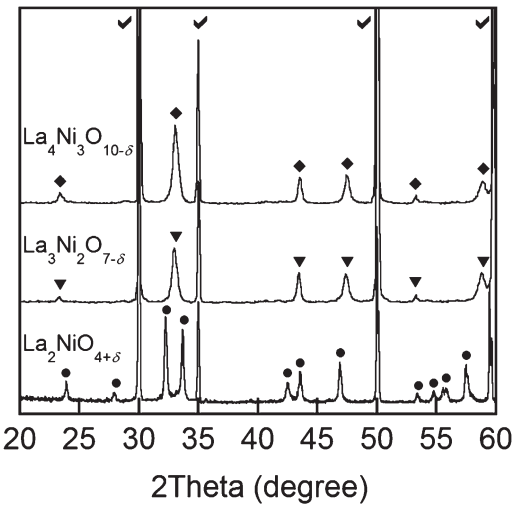


**Fig. 2** XRD patterns of $La_{n+1}Ni_nO_{3n+1}$ ($n$ = 1, 2, and 3)–YSZ sintered at 1123 K: each symbol indicates $La_{n+1}Ni_nO_{3n+1}$ ($n$ = 1, 2, and 3), $La_2NiO_{4+\delta}$ (•), $La_3Ni_2O_{7-\delta}$ (▼), $La_4Ni_3O_{10-\delta}$ (♦), and YSZ (✓).

titration[14,15] as a function of $p(O_2)$ in a temperature range of 923–1023 K. In general, oxygen interstitials ($O_i''$) are considered the dominating defects for $n$ = 1 whereas oxygen vacancies ($V_o^{\bullet\bullet}$) are the main defects for $n$ = 2 and 3 due to the increase of perovskite layers in the structure.

There is a considerable change in oxygen non-stoichiometry throughout the $p(O_2)$ range for all compounds. The data show that the isotherms of $La_{n+1}Ni_nO_{3n+1}$–YSZ ($n$ = 1, 2, and 3) have similar shapes, suggesting that the reduction mechanisms of the scaffolds are quite similar. As temperature decreases, the decomposition $p(O_2)$ becomes lower. With an increase of $n$, the isotherms are extended to the left, indicating that $La_4Ni_3O_{10-\delta}$ has higher redox stability than $La_2NiO_{4+\delta}$ down to a lower $p(O_2)$ at the same temperature. This is due possibly to the higher number of perovskite layers in $La_4Ni_3O_{10-\delta}$ and, accordingly, stronger interaction between the molecules in the lattice.

The partial molar enthalpy and entropy of oxygen can be calculated from the slopes of the isotherms. The Gibbs free energy, $\Delta G$, is related to the equilibrium constant, $K$, and $p(O_2)$ as follows,

$$\Delta G = -RT\ln K = \frac{1}{2}RT\ln p(O_2) \quad (1)$$

At a constant $\delta$, the partial molar enthalpy of oxygen at various temperatures is shown by the Gibbs–Helmholtz equation.

$$\Delta H = \frac{\partial\left(\frac{\Delta G}{T}\right)}{\partial\left(\frac{1}{T}\right)} = \frac{R}{2}\frac{\partial \ln[p(O_2)]}{\partial\left(1/T\right)}\bigg|_{\delta} \quad (2)$$

And the partial molar entropy can be obtained by using the Maxwell relation as follows.

$$-\Delta S = \frac{\partial \Delta G}{\partial T} = \left(\frac{R}{2}\right)\left(\frac{\partial T\ln p(O_2)}{\partial T}\right)\bigg|_{\delta} \quad (3)$$

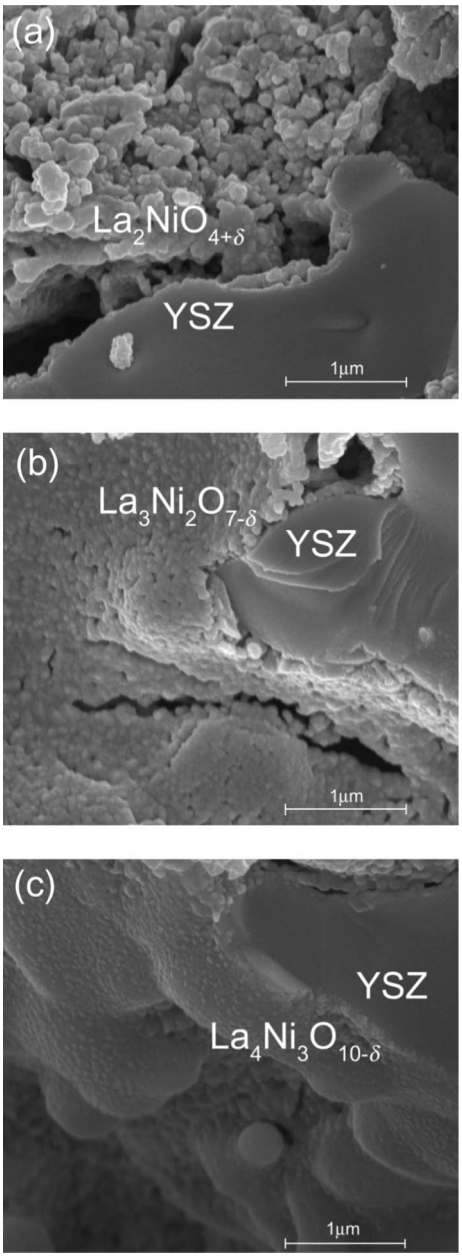


**Fig. 3** SEM images of the (a) $La_2NiO_{4+\delta}$–YSZ, the (b) $La_3Ni_2O_{7-\delta}$–YSZ, and the (c) $La_4Ni_3O_{10-\delta}$–YSZ annealed at 1123 K.

The partial enthalpies of oxidation for the $La_{n+1}Ni_nO_{3n+1}$–YSZ ($n$ = 1, 2, and 3), calculated from eqn (2), are presented in Fig. 5. The oxidation enthalpies ($-\Delta H$) are a strong function of oxygen non-stoichiometry in $La_{n+1}Ni_nO_{3n+1}$ ($n$ = 1, 2, and 3).

The partial molar enthalpies of oxidation at $10^{-5}$ atm are plotted in Fig. 6. The higher partial molar enthalpy for $La_4Ni_3O_{10-\delta}$–YSZ relative to that of $La_{n+1}Ni_nO_{3n+1}$ ($n$ = 1 and 2) means that it would be more stable at roughly the same $p(O_2)$.

**2.1 Hyperstoichiometric $La_2NiO_{4+\delta}$.** The partial molar enthalpies of oxidation for the $La_2Ni_1O_{4+\delta}$–YSZ ranges from −20 to −250 kJ mol$^{-1}$. The values of $-\Delta H$ become smaller for larger $\delta$, implying a lower energy is needed for the formation of one interstitial oxygen. Oxidation of the nickel ions in the lattice

 

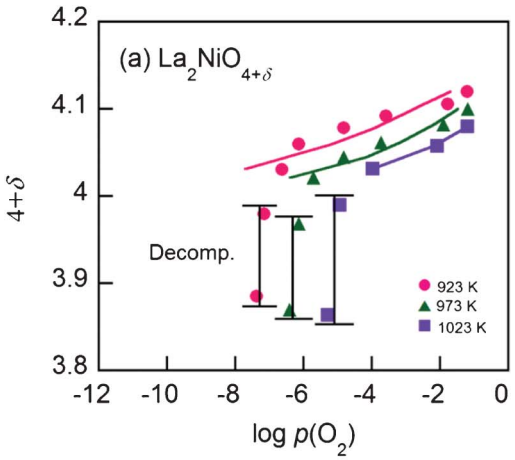


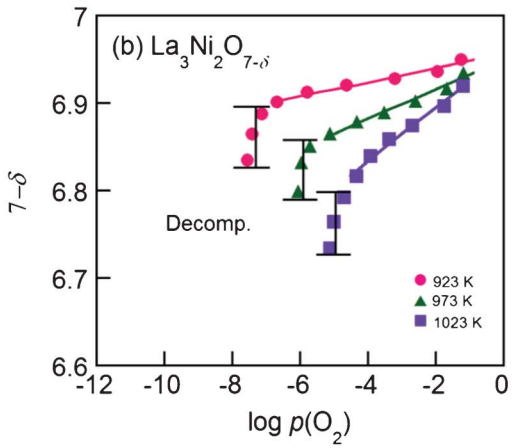


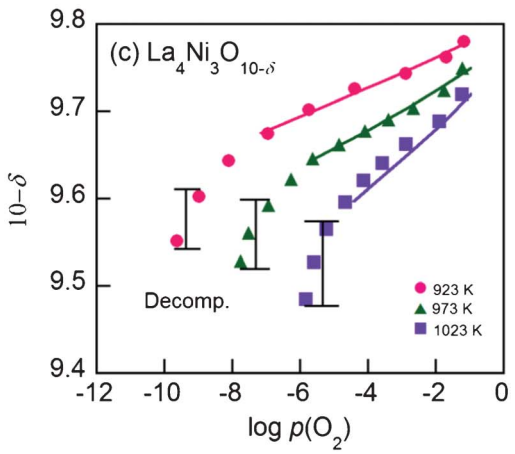


**Fig. 4** The isotherms of the $La_{n+1}Ni_nO_{3n+1}$ ($n$ = 1, 2, and 3)–YSZ at 923–1023 K, (a) $La_2NiO_{4+\delta}$, (b) $La_3Ni_2O_{7-\delta}$ and (c) $La_4Ni_3O_{10-\delta}$. The solid curves are fitting curves calculated by the proposed defect model using data only before decomposition.

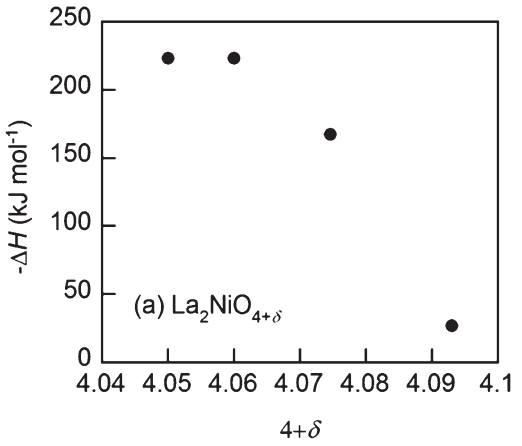


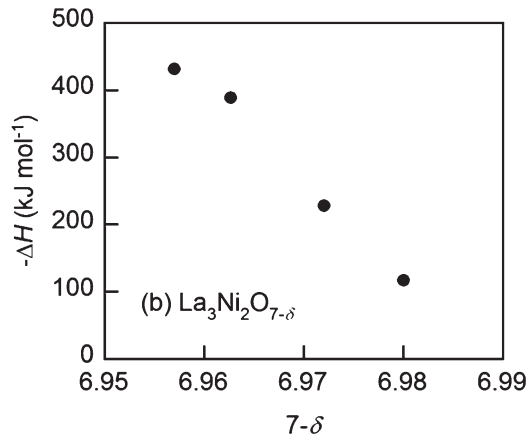


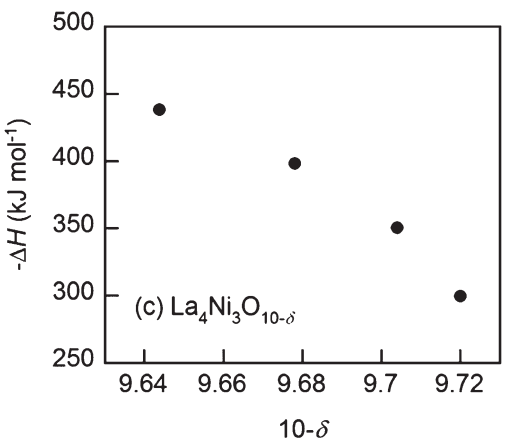


**Fig. 5** Partial molar enthalpy of oxidation ($-\Delta H$) at 973 K of the $La_{n+1}Ni_nO_{3n+1}$ ($n$ = 1, 2, and 3)–YSZ, (a) $La_2NiO_{4+\delta}$, (b) $La_3Ni_2O_{7-\delta}$ and (c) $La_4Ni_3O_{10-\delta}$.

would then destabilize the local structure near the defected sites. In other words, the interatomic forces between ions inside the lattice may become weaker in the vicinity of the defected sites.

The partial molar entropies of oxidation, calculated from the differences in the Gibbs free energies and the enthalpies, are presented in Fig. 7. The values of $-\Delta S$ become smaller for higher $\delta$, implying that the probability for interstitial oxygen formation decreases with excess oxygen. In other words, there are fewer sites for the interstitial oxygen formation reaction in the scaffolds as the amount of excess oxygen increases (Fig. 7a).[9,15–17]

**2.2 Oxygen deficient $La_3Ni_2O_{7-\delta}$ and $La_4Ni_3O_{10-\delta}$.** The partial molar enthalpies of oxidation for the $La_{n+1}Ni_nO_{3n+1}$–YSZ ($n$ = 2, and

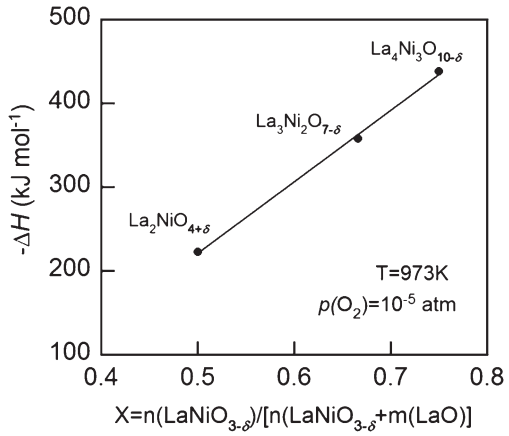


**Fig. 6** Partial molar enthalpy of oxidation ($-\Delta H$) at 973 K of the $La_{n+1}Ni_nO_{3n+1}$ ($n$ = 1, 2, and 3)–YSZ at $p(O_2) = 10^{-5}$ atm.

3) range from −100 to −430 kJ mol$^{-1}$ and −300 to −450 kJ mol$^{-1}$, respectively. However, the values of $-\Delta H$ become larger for higher $\delta$, implying higher energy is needed for release of the oxygen inside the lattice (*i.e.* oxygen vacancy formation) as the reduction proceeds.

It can also be argued that fewer sites will be available for oxygen vacancy formation in the scaffolds as the concentration of oxygen vacancies increases. This is consistent with the finding that the values of $-\Delta S$ become smaller for higher $\delta$ (Fig. 7b and c).[9,18]

## 3. Defect analysis

**3.1 Hyperstoichiometric $La_2NiO_{4+\delta}$.** The predominant point defects in $La_2NiO_{4+\delta}$ are, expectedly, oxygen interstitials $O_i''$ and electron holes.[19] The concentration of oxygen vacancies is considered negligible here. The following pseudo-chemical reaction shows the equilibrium between oxygen interstitials, electron holes, and the surrounding oxygen gas molecules.

$$\frac{1}{2}O_2(g) \leftrightarrow O_i'' + 2h^{\bullet} \quad (4)$$

Thus, electroneutrality approximation requires that the number of electron holes should be about twice the number of oxygen interstitials.

$$[h^{\bullet}] = 2[O_i''] = 2\delta \quad (5)$$

In terms of $\delta$ and $p(O_2)$, the equilibrium constant for eqn (4) can be expressed as

$$K = \frac{[O_i''][h^{\bullet}]^2}{p(O_2)^{1/2}}\gamma_1\gamma_2{}^2 = \frac{(\delta)(2\delta)^2}{p(O_2)^{1/2}}\gamma_1\gamma_2{}^2 \quad (6)$$

where $\gamma_1$ and $\gamma_2$, denote the activity coefficients of $O_i''$ and $h^{\bullet}$, respectively.

Thus, the Gibbs free energy change for eqn (4) can be expressed as follows.

$$\Delta G = -RT\ln K = -RT\ln\frac{(\delta)(2\delta)^2}{p(O_2)^{1/2}} - RT\ln(\gamma_1\gamma_2{}^2) \quad (7)$$

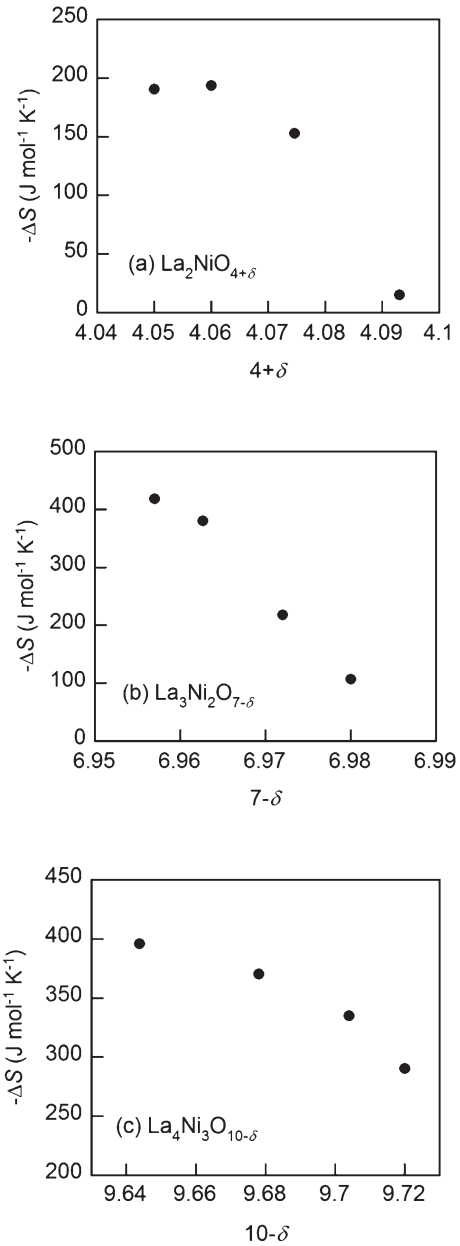


**Fig. 7** Partial molar entropy of oxidation ($-\Delta S$) at 973 K of the $La_{n+1}Ni_nO_{3n+1}$ ($n$ = 1, 2, and 3)–YSZ, (a) $La_2NiO_{4+\delta}$, (b) $La_3Ni_2O_{7-\delta}$ and (c) $La_4Ni_3O_{10-\delta}$.

The second term in eqn (7) represents the deviation from the Gibbs free energy change for an ideal system (activity coefficient = 1). As a first order approximation, the deviation is assumed to be a linear function of the oxygen non-stoichiometry, $\delta$.[16,19]

$$\Delta G_{ex} = -RT\ln\gamma_1\gamma_2{}^2 \equiv a\delta \quad (8)$$

Thus, the constant $a$ reflects the degree of interaction between the defects and the lattice ions. A positive $a$ suggests that the formation of interstitial oxygen is easier than in an ideal system while a negative $a$ implies that it becomes more difficult than in an ideal system.[16] As $a$ approaches zero, the system reduces to the ideal system (*i.e.* there is no interactions between the defects and the lattice ions). In light of eqn (8), eqn (7) can be rewritten as

 

$$p(O_2) = \frac{16\delta^6}{K^2}\left\{\exp\left(\frac{-a\delta}{RT}\right)\right\}^2 \quad (9)$$

The relationship between $\delta$ and $p(O_2)$ as described by eqn (9) can then be used to estimate the parameters $K$ and $a$ from experimental data.

The formation of oxygen interstitials in $La_2NiO_{4+\delta}$–YSZ is electrically compensated by the formation of electron holes to satisfy electroneutrality. The oxygen non-stoichiometry data for all $La_2NiO_{4+\delta}$–YSZ were fitted to the models described above. The theoretical curves calculated for $La_2NiO_{4+\delta}$–YSZ using eqn (9) are presented as solid lines in Fig. 4(a), with the fitted $K$ and $a$ values listed in Table 1. Although there was some small deviation, the observed non-stoichiometric behaviour of $La_2NiO_{4+\delta}$–YSZ can be well explained using the proposed defect model over a wide range of $p(O_2)$ except the area where decomposition is expected. The equilibrium constant $K$ increases exponentially with temperature, implying that the formation of oxygen interstitials is highly affected by temperature, as also shown in the isotherms. This is further confirmed by the observation that the slope of $\delta$ *versus* $p(O_2)$ at higher temperatures is steeper than that at lower temperatures, reflecting the relative ease of interstitial oxygen formation at high temperatures.

Since the value of $-a$ for $La_2NiO_{4+\delta}$–YSZ decreases with increasing temperature, the degree of interactions between the defects and the lattice ions diminishes at higher temperatures.

**3.2 Oxygen deficient $La_3Ni_2O_{7-\delta}$ and $La_4Ni_3O_{10-\delta}$.** Since oxygen vacancies ($V_O^{\bullet\bullet}$) and electron holes are the dominant defects in these crystals, the interactions between the crystal and the surrounding oxygen molecules can be described as follows.

$$\frac{1}{2}O_2 + V_O^{\bullet\bullet} \xleftrightarrow{K} O_O^X + 2h^\bullet \quad (10a)$$

where the electron holes can be emitted from the lattice ions (most likely Ni ions) as follows,

$$Ni_{Ni}^X \leftrightarrow Ni_{Ni}' + h^\bullet \quad (10b)$$

The combination of eqns (10a) and (10b) are the dominant defect reaction in these materials. Thus, charge neutrality requires that the effective negative charge on the lattice ions be balanced by the positive charges of electron holes and oxygen vacancies, as described below.

$$[Ni_{Ni}'] = [h^\bullet] + 2[V_O^{\bullet\bullet}] \text{ or } [h^\bullet] = [Ni_{Ni}'] - 2\delta \quad (11)$$

**Table 1** The fitting parameters providing the best fit to the measurements ($La_2NiO_{4+\delta}$)

| $La_2NiO_{4+\delta}$ | log K | $a$ (J mol$^{-2}$) |
|---|---|---|
| 923 K | 0.336 | −2.42 E+05 |
| 973 K | −1.130 | −9.88 E+04 |
| 1023 K | −1.792 | −7.68 E+04 |

Here, the concentration of the charged lattice ions changes with non-stoichiometry as well. Since the electronic conductivity ($\sigma_h$) is much greater than the ionic conductivity ($\sigma_v$) for these materials, however, the total conductivity ($\sigma$) is dominated primarily by the transport of electron holes, *i.e.*

$$\sigma \approx \sigma_h + \sigma_v \approx \sigma_h \approx [h^\bullet]\mu_h q \text{ or } [h^\bullet] \approx \frac{\sigma}{\mu_h q} \quad (12)$$

where $q$ is the charge of electron and $\mu_h$ is the drift mobility of electron holes.

In light of this approximation, the equilibrium constant for eqn (10a) can be approximated by

$$K = \frac{[O_o^x][h^\bullet]^2}{p(O_2)^{1/2}[V_o^{\bullet\bullet}]}\frac{\gamma_3{\gamma_2}^2}{\gamma_4} = \frac{[O_o^x]\left(\frac{\sigma}{q\mu_h}\right)^2}{p(O_2)^{1/2}[V_o^{\bullet\bullet}]}\frac{\gamma_3{\gamma_2}^2}{\gamma_4} \quad (13)$$

where $\gamma_3$ and $\gamma_4$ denote the activity coefficients of $O_o^x$ and $V_o^{\bullet\bullet}$, respectively.

The Gibbs free energy change, $\Delta G$, of eqn (10a) can be expressed in terms of the equilibrium constant, $K$, as in eqn (14a) and (14b) for $La_3Ni_2O_{7-\delta}$ and $La_4Ni_3O_{10-\delta}$, respectively.

$$\Delta G = -RT\ln K = -RT\ln\frac{(7-\delta)\left(\frac{\sigma}{q\mu_h}\right)^2}{p(O_2)^{1/2}\delta} - RT\ln\left(\frac{\gamma_3{\gamma_2}^2}{\gamma_4}\right) \quad \text{for } La_3Ni_2O_{7-\delta} \quad (14a)$$

$$\Delta G = -RT\ln K = -RT\ln\frac{(10-\delta)\left(\frac{\sigma}{q\mu_h}\right)^2}{p(O_2)^{1/2}\delta} - RT\ln\left(\frac{\gamma_3{\gamma_2}^2}{\gamma_4}\right) \quad \text{for } La_4Ni_3O_{10-\delta} \quad (14b)$$

We define the second term in eqn (14a) and (14b) as the deviation from the standard free energy change of the ideal system, similar to the approximation made for the $La_2NiO_{4+\delta}$ case.[20]

$$\Delta G_{ex} = RT\ln\frac{\gamma_3{\gamma_2}^2}{\gamma_4} \equiv a\delta \quad (15)$$

Solving eqn (13)–(15) simultaneously with $K^* \equiv K(q\mu_h)^2$, we have following equations.

$$K^* = \frac{(7-\delta)\sigma^2}{p(O_2)^{1/2}\delta}\frac{\gamma_3{\gamma_2}^2}{\gamma_4} \quad \text{for } La_3Ni_2O_{7-\delta} \quad (16a)$$

$$K^* = \frac{(10-\delta)\sigma^2}{p(O_2)^{1/2}\delta}\frac{\gamma_3{\gamma_2}^2}{\gamma_4} \quad \text{for } La_3Ni_3O_{10-\delta} \quad (16b)$$

which can be rewritten as,

$$p(O_2) = \frac{(7-\delta)^2\sigma^4}{K^{*2}\delta^2}\left\{\exp\left(\frac{a\delta}{RT}\right)\right\}^2 \quad \text{for } La_3Ni_2O_{7-\delta} \quad (17a)$$

**Table 2** The fitting parameters providing the best fit to the measurements ($La_3Ni_2O_{7-\delta}$, and $La_4Ni_3O_{10-\delta}$)

| $La_3Ni_2O_{7-\delta}$ | log $K^*$ | $a$ (J mol$^{-2}$) | $La_4Ni_3O_{10-\delta}$ | log $K^*$ | $a$ (J mol$^{-2}$) |
|---|---|---|---|---|---|
| 923 K | 1.308 | −8.53 E+05 | 923 K | 0.049 | −4.13 E+05 |
| 973 K | 1.662 | −4.27 E+05 | 973 K | 0.412 | −3.15 E+05 |
| 1023 K | 1.959 | −2.17 E+05 | 1023 K | 1.112 | −1.89 E+05 |

$$p(O_2) = \frac{(10-\delta)^2\sigma^4}{K^{*2}\delta^2}\left\{\exp\left(\frac{a\delta}{RT}\right)\right\}^2 \quad \text{for } La_4Ni_3O_{10-\delta} \qquad (17b)$$

The oxygen non-stoichiometry data ($\delta$ values) and the electrical conductivity data ($\sigma$ values) at different partial pressures of oxygen collected for the two cathodes ($La_3Ni_2O_{7-\delta}$–YSZ and $La_4Ni_3O_{10-\delta}$–YSZ) were curve fitted to the models again. The theoretical curves calculated for using eqn (17a) and (17b) are presented as solid lines in Fig. 4(b) and 4(c), respectively, with the fitted $K^*$ and $a$ values listed in Table 2. The theoretical curves again show quite good agreement with the experimental data before decomposition. Oxygen vacancy formation becomes more difficult compared to the ideal system when $a$ is negative.[20,21]

## 4. Electrical conductivity

Shown in Fig. 8 are electrical conductivities for the $La_{n+1}Ni_nO_{3n+1}$–YSZ ($n$ = 1, 2, and 3). At a given temperature, electrical conductivity increased with the value of $n$, due possibly to the increased number of Ni–O–Ni interactions, which are responsible for the electronic conduction pathways in the perovskite layers.[12] In other words, the conductivity arises mostly from the oxidation state of Ni ions and their electronic configuration. Stoichiometric $La_2NiO_{4+\delta}$ has a stable $Ni^{2+}$ oxidation state, whereas incorporation of oxygen interstitials are compensated by $Ni^{3+}$. Therefore, the electronic conductivity in R–P lanthanum nickelate series depends on the increasing $Ni^{3+}/Ni^{2+}$ ratio with $n$, along with the particular connectivity of Ni ions in the structure.[22,23] However, the electrical conductivity showed a different trend on temperature. The electrical

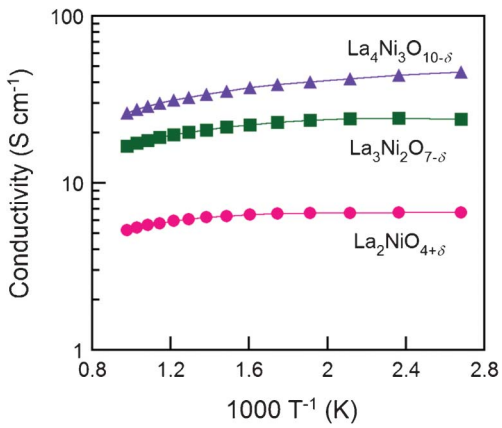


**Fig. 8** The electrical conductivity of $La_{n+1}Ni_nO_{3n+1}$ ($n$ = 1, 2, and 3)–YSZ at various temperatures from 1023 K to 373 K in air, (●) $La_2NiO_{4+\delta}$, (■) $La_3Ni_2O_{7-\delta}$, and (▲) $La_4Ni_3O_{10-\delta}$.

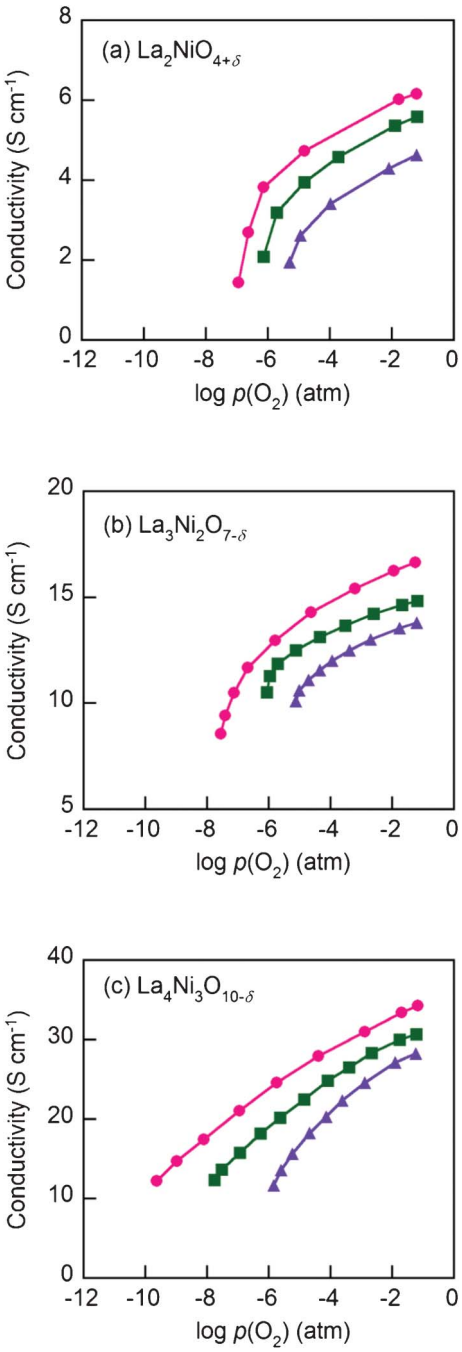


**Fig. 9** The electrical conductivities of $La_{n+1}Ni_nO_{3n+1}$ ($n$ = 1, 2, and 3)–YSZ, (a) $La_2NiO_{4+\delta}$, (b) $La_3Ni_2O_{7-\delta}$, and (c) $La_4Ni_3O_{10-\delta}$ at (●) 923 K, (■) 973 K, and (▲) 1023 K at various $p(O_2)$ (atm).

conductivities of $La_2NiO_{4+\delta}$–YSZ ($n$ = 1) and $La_3Ni_2O_{7-\delta}$–YSZ ($n$ = 2) show little dependence on temperature below ~573 K and then decreased slightly with increasing temperature ($573 < T$ (K) $< 1023$). On the contrary, the electrical conductivity of $La_4Ni_3O_{10-\delta}$–YSZ ($n$ = 3) decreased monotonically with temperature, showing metallic behavior over the entire temperature range. The electrical conductivities for $La_{n+1}Ni_nO_{3n+1}$ (42 wt%)–YSZ ($n$ = 1, 2, and 3) calcined at 1023 K as a function of $p(O_2)$ at various temperatures ($923 < T$ (K) $< 1023$) are presented in Fig. 9. The electrical conductivities

 

increased with $p(O_2)$ in all cases over the entire temperature range studied, indicating that this material is a *p*-type electronic conductor under the testing conditions. Further, the electrical conductivities measured at a higher temperature changed more rapidly with $p(O_2)$, suggesting that the electrical properties are more sensitive to oxygen non-stoichiometry at higher temperatures.

For $La_2NiO_{4+\delta}$, the electrical conductivities increased with $p(O_2)$ due mainly to increased concentration of mobile interstitial oxygen in the perovskite layers. Since the predominant defects in $La_2NiO_{4+\delta}$ are interstitial oxygen and electronic holes, an increase in the concentration of oxygen interstitial results in an increase in the concentration of electronic holes, which leads to increased electronic conductivity of the material.[14,15]

For $La_3Ni_2O_{7-\delta}$ and $La_4Ni_3O_{10-\delta}$, in contrast, an increase in oxygen partial pressure would lead to a decrease in concentration of oxygen vacancies and an increase in the concentration of electronic holes, which in turn increase the *p*-type electrical conductivity.

## Conclusion

$La_{n+1}Ni_nO_{3n+1}$ ($n$ = 1, 2, and 3) were infiltrated into scaffolds of YSZ to form porous cathodes for IT-SOFCs. The redox properties of $La_{n+1}Ni_nO_{3n+1}$ ($n$ = 1, 2, and 3) infiltrated in YSZ were investigated using coulometric titration. $La_4Ni_3O_{10-\delta}$ appears to be more suited as cathode materials than $La_2NiO_{4+\delta}$ and $La_3Ni_2O_{7-\delta}$ because it has higher oxidation enthalpies and hence better stability in a lower $p(O_2)$ under the same testing conditions, Partial molar entropies can provide insight into the variation of the number of sites available for oxygen interstitial or vacancy formation reactions during the oxidation/reduction process. A defect model is proposed and it fits well the experimental data on non-stoichiometric variations of oxygen over a wide range of $p(O_2)$. All samples show increased electrical conductivity with increasing $n$ at a given temperature. Therefore, the $La_4Ni_3O_{10-\delta}$–YSZ is considered the most favorable candidate cathode material for IT-SOFC applications.

## Acknowledgements

This research was supported by the WCU (World Class University) program (R31-2009-000-20012-0) and the Basic Science Research Program (2011-0010773) through the National Research Foundation of Korea funded by the Ministry of Education, Science and Technology, and the New & Renewable Energy of the Korea Insitute of Energy Technology Evaluation and Planning (KETEP) grant (20113020030060) funded by the Korea government Ministry of Knowledge Economy.

## References

1 A. J. Jacobson, *Chem. Mater.*, 2010, **22**, 660.
2 G. Amow and S. J. Skinner, *J. Solid State Electrochem.*, 2006, **10**, 538.
3 Z. Zhang, M. Greenblatt and J. B. Goodenough, *J. Solid State Chem.*, 1994, **108**, 402.
4 Z. Zhang and M. Greenblatt, *J. Solid State Chem.*, 1995, **117**, 236.
5 K. T. Lee and A. Manthiram, *Chem. Mater.*, 2006, **18**, 1621.
6 G. Amow, I. J. Davidson and S. J. Skinner, *Solid State Ionics*, 2006, **177**, 1205.
7 S. J. Skinner and J. A. Kilner, *Solid State Ionics*, 2000, **135**, 709.
8 A. Yamada, Y. Suzuki, K. Saka, M. Uehara, D. Mori, R. Kanno, T. Kiguchi, F. Mauvy and J. C. Grenier, *Adv. Mater.*, 2008, **20**, 4124.
9 D. O. Bannikov, A. P. Safronov and V. A. Cherepanov, *Thermochim. Acta*, 2006, **451**, 22.
10 Z. Gao, Z. Q. Mao, C. Wang and Z. X. Liu, *Int. J. Hydrogen Energy*, 2010, **35**, 12905.
11 V. V. Kharton, A. P. Viskup, E. N. Naumovich and F. M. B. Marques, *J. Mater. Chem.*, 1999, **9**, 2623.
12 E. V. Tsipis, M. V. Patrakeev, J. C. Waerenborgh, Y. V. Pivak, A. A. Markov, P. Gaczynski, E. N. Naumovich and V. V. Kharton, *J. Solid State Chem.*, 2007, **180**, 1902.
13 M. Andersson, J. L. Yuan and B. Sunden, *Appl. Energy*, 2010, **87**, 1461.
14 S. Yoo, J. Y. Shin and G. Kim, *J. Mater. Chem.*, 2011, **21**, 439.
15 S. Yoo, J. Y. Shin and G. Kim, *J. Electrochem. Soc.*, 2011, **158**, B632.
16 T. Nakamura, K. Yashiro, K. Sato and J. Mizusaki, *Solid State Ionics*, 2009, **180**, 368.
17 E. V. Tsipis, E. N. Naumovich, M. V. Patrakeev, J. C. Waerenborgh, Y. V. Pivak, P. Gaczynski and V. V. Kharton, *J. Phys. Chem. Solids*, 2007, **68**, 1443.
18 S. Sengodan, H. J. Yeo, J. Y. Shin and G. Kim, *J. Power Sources*, 2011, **196**, 3083.
19 Z. Li, R. Haugsrud, J. B. Smith and T. Norby, *Solid State Ionics*, 2009, **180**, 1433.
20 S. Onuma, K. Yashiro, S. Miyoshi, A. Kaimai, H. Matsumoto, Y. Nigara, T. Kawada, J. Mizusaki, K. Kawamura, N. Sakai and H. Yokokawa, *Solid State Ionics*, 2004, **174**, 287.
21 M. Oishi, K. Yashiro, J. O. Hong, Y. Nigara, T. Kawada and J. Mizusaki, *Solid State Ionics*, 2007, **178**, 307.
22 M. D. Carvalho, A. Wattiaux, L. P. Ferreira and J. M. Bassat, *J. Solid State Chem.*, 2009, **182**, 60.
23 M. Schroeder and M.-A. Dragan, *J. Mater. Sci.*, 2007, **42**, 1972.